ISSN: 2634 - 8853

Journal of Engineering and Applied Sciences Technology

SCIENTIFIC Research and Community

Research Article

Open Access

Dual Solutions of Casson Tetra Hybrid Nanofluid Flow with Homogenous-Heterogenous Reactions in a Porous Curved Surface with the Inclusion of Deformable Roughness

Rakesh MHP

Department of Mathematics Government Science College, Gandhinagar, India

ABSTRACT

- This study investigates thermal conductivity enhancement and improved heat transfer performance, which are vital in advanced industrial processes, engineering applications, and electronics cooling systems.
- A stability analysis is conducted for dual solutions of Casson tetra-hybrid nanofluid flow over a porous curved surface in the presence of homogeneous and heterogeneous reactions.
- The non-Newtonian Casson model, integrated with the Tiwari–Das nanoparticle formulation, is utilized to analyze the influence of nanoparticle volume fraction, Darcy–Forchheimer drag, nonlinear mixed convection, magnetic field, mass suction/injection, slip effects, and convective boundary conditions on the velocity, temperature, and concentration distributions, as well as on skin friction and Nusselt number behavior.
- Similarity transformations are applied to convert the governing equations into a system of nonlinear ordinary differential equations, which are then solved using the MATLAB bvp4c numerical solver.
- The findings reveal that the Forchheimer drag, slip velocity, and Casson parameters exhibit similar effects on velocity, whereas mixed and nonlinear convection parameters demonstrate opposing effects.
- Tetra-hybrid nanofluids provide significantly greater heat transfer improvement than hybrid and tri-hybrid nanofluids. Enhancements in homogeneous and heterogeneous reaction parameters lead to a reduction in the dual concentration solutions.
- Moreover, the first solution of the skin friction coefficient decreases, while the dual Nusselt number solutions increase under the effects of mass suction/injection, local porosity, mixed convection, slip velocity, and Casson parameters.
- Stability analysis confirms the physical reliability of the first solution and the instability of the second solution.
- Grid independence checks and strong agreement with previously published data further validate the accuracy and robustness of the numerical results.

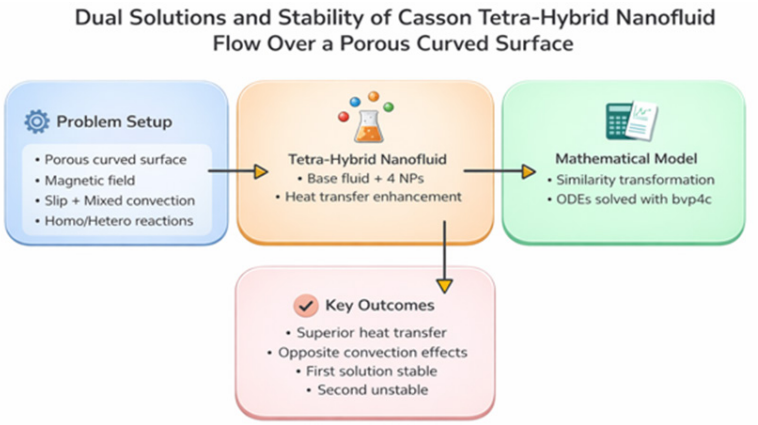

***Corresponding author**

Rakesh Manilal H. Patel, Department of Mathematics, Government Science College, Gandhinagar, India. Email: rmpatel2711@gmail.com

Received: April 17, 2026; **Accepted:** May 22, 2026; **Published:** May 31, 2026

Keywords: Casson Tetra-Hybrid Nanofluid, Porous Curved Surface, Dual Solutions, Stability Analysis, Similarity Transformation, Darcy-Forchheimer Model, Nonlinear Mixed Convection, Slip Boundary Condition, Homogeneous–Heterogeneous Reactions, Heat Transfer Enhancement, Non-Newtonian Fluid Flow, Nusselt Number Behavior

Subject Classification

EEE / Engineering-based journals (generalized): • Heat Transfer and Thermal Engineering • Computational Fluid Dynamics • Nanofluid Technology • Porous Media Flow • Non-Newtonian Fluid Mechanics • Chemical Reaction Engineering Elsevier / Scopus ASJC Codes: • 2210-Mechanical Engineering • 1506 - Materials Science (Composites & Nanomaterials) • 2207 –

Fluid Flow and Transfer Processes • 1502-Energy Engineering and Power Technology • 2502-Modeling and Simulation • 1605-Applied Mathematics Mathematics Subject Classification (MSC 2020): • 76A05-Non-Newtonian fluids • 76S05-Flows in porous media • 80A20- Heat and mass transfer, heat flow • 65L10-Numerical solution of boundary value problems • 35Q35-PDEs in connection with fluid mechanics…

Nomenclature

Symbol	Description
a	Constant
u, v	Velocity components along the surface and normal directions
s, r	Spatial coordinates
R	Radius of curvature
t	Time coordinate
T	Temperature field
Bi	Thermal Biot number
K	Curvature parameter
Gr	Local Grashof number
P	Pressure
M	Magnetic parameter
F_r	Forchheimer number
P_r	Prandtl number
K_m	Heterogeneous reaction parameter
K_n	Homogeneous reaction parameter
S	Mass suction/injection parameter
Sc	Schmidt number
λ	Casson parameter
λ_T	Mixed convection parameter
ω	Nonlinear convection parameter
σ	Electrical conductivity
μ	Dynamic viscosity of the fluid
Cp	Specific heat at constant pressure
ρ	Density of the fluid
k	Thermal conductivity of the fluid
Kp	Porous medium permeability
ζ	Dimensionless similarity variable
f′(ζ)	Dimensionless velocity profile
θ(ζ)	Dimensionless temperature profile
ϕ(ζ)	Dimensionless concentration profile
Re	Local Reynolds number
C_{fs}	Local skin friction coefficient
N_{us}	Local Nusselt number
ϕCu, ϕTiO_2, ϕAg, ϕAl_2O_2	Nanoparticle volume fractions of Cu, TiO_2, Ag, and Al_2O_3 respectively
$(\sigma ec)_{thnf}$	Electrical conductivity of tetra-hybrid nanofluid
(β)thnf	Thermal expansion coefficient of tetra-hybrid nanofluid
kthnf	Thermal conductivity of tetra-hybrid nanofluid
(ρCp)thnf	Heat capacity of tetra-hybrid nanofluid
μthnf	Dynamic viscosity of tetra-hybrid nanofluid
Subscript	**Meaning**
tethnf	Tetra-hybrid nanofluid
hnf	Hybrid nanofluid
trihnf	Tri-hybrid nanofluid
nf	Nanofluid
f	Base fluid
w	At the wall
∞	Ambient/free stream condition

Introduction

Non-Newtonian fluids exhibit a nonlinear relationship between shear stress and shear rate, unlike Newtonian fluids in which viscous stress varies linearly with the local strain rate. Due to these nonlinear characteristics, classical Newtonian models often fail to accurately describe many industrial fluids such as paints, shampoos, polymer solutions, emulsions, and even biological fluids like blood. To better capture these complex flow behaviors, numerous non-Newtonian models have been developed, including the Maxwell, Brinkman-type, Jeffrey, Walter-B, viscoplastic, and Oldroyd-B fluid models. Among these, the Casson model, originally proposed by Casson, is widely used to characterize pseudoplastic (shear-thinning) behavior [1]. Casson fluids exhibit elevated viscosity at low shear rates, which progressively decreases as shear rate rises. These properties make Casson fluids highly suitable for applications in pharmaceuticals, cosmetics, chemical and food processing, including the manufacturing of oils, syrups, beverages, detergents, and deodorizing products. Given its practical relevance, Casson fluid flow has been the subject of extensive research. Dash et al. examined Casson flow in porous pipe media, while Deebani et al. [2]. studied magneto-radiative Casson nanofluid behavior over stretching/shrinking cylindrical geometries. Varun et al [3]. investigated chemically reacting magnetohydrodynamic Casson nanofluid flow over curved stretching surfaces, and Bhargavi et al [4]. focused on hydromagnetic Casson nanofluid heat transport with slip effects over curved boundaries [5]. Nanotechnology involves the development and application of materials with characteristic dimensions typically below 100 nm. Nanomaterials are commonly classified into carbon-based, metal-based, dendrimer-based, and composite forms [6]. Choi introduced the concept of nanofluids, defined as base fluids dispersed with metallic or nonmetallic nanoparticles at extremely small scales [7]. Nanofluids have gained significant attention due to their ability to enhance thermal performance in electronics cooling, renewable energy systems, heat exchangers, and automotive engineering. To analyze nanofluid heat and mass transfer behavior, the Tiwari-Das model is one of the most widely used frameworks. It incorporates nanoparticle volume fraction and enhanced thermal conductivity effects, enabling accurate prediction of heat transfer performance [8]. This model is particularly relevant for tetra-hybrid nanofluids consisting of four distinct nanoparticle types. Asghar et al. for example, used the model to study hybrid nanofluids under Joule heating conditions, highlighting its capability in practical engineering systems including biomedical devices and industrial cooling [9]. Further developments include analyses of convective heat transfer and Lorentz force influences on ternary-hybrid nanofluids over curved surfaces, and studies of magnetized hybrid nanofluids containing gyrotactic microorganisms with slip effects [10-11]. Fluid flow through porous media is frequently encountered in industrial filtration, geophysical flows, and mechanical structures such as foams and packed beds. Darcy's law predicts flow behavior assuming linear pressure-velocity

relationships. However, this assumption fails at high velocities or in irregular porous geometries. The Darcy-Forchheimer formulation incorporates inertial corrections to address such nonlinearities [12]. Various studies have integrated this approach with advanced fluid models, including micropolar ferrofluids, Casson fluids, magnetized nanofluids with slip, hybrid nanofluids over curved surfaces, and rotating hybrid nanofluids under thermal radiation and convective boundary effects [13-19]. Chemical reactions in fluid flows often involve simultaneous homogeneous (bulk-phase) and heterogeneous (surface-catalyzed) processes, relevant in catalysis, polymer manufacturing, combustion, food processing, and energy systems. Choudhary and Merkin first examined boundary-layer flows incorporating both reactions [20]. Later, several researchers extended such studies to Casson fluids with suction/injection and slip effects, Darcy-Forchheimer flows with entropy generation, and hybrid nanofluids subjected to induced magnetic fields over curved surfaces [21-23]. Curved surfaces play a significant role in heat and momentum transfer for aerospace and automotive structures, turbine blades, and aerodynamic components. Curvature modifies pressure gradients, vortex structures, and boundary layer thickness. Mishra et al. compared the behavior of two hybrid nanofluids, (Ag-MgO)/H_2O and (Fe_3O_4-$CoFe_2O_4$)/H_2O, across curved geometries, while Wahid et al [24]. studied magnetized hybrid nanofluids over exponentially stretching/shrinking curved surfaces [25]. Nonlinear mixed convection arises from combined forced and natural convection effects, leading to complex flow interactions that strongly influence mass and heat transport. Pandey et al. and Patil et al [26]. provided significant insights into nonlinear mixed convection in various configurations [27]. Multiple (dual) solutions are known to arise in nonlinear boundary-layer flows under certain geometrical or thermal constraints. Dual or multiple solutions have been reported for hybrid nanofluids over curved surfaces and are frequently accompanied by contrasting stability characteristics [28-35]. Despite significant progress, the stability analysis of tetra-hybrid nanofluid flow over curved geometries remains largely unexplored. Previous work has focused on hybrid and trihybrid nanofluids, revealing a clear research gap [36-37]. This study addresses that gap by performing a comprehensive stability analysis of Casson tetra-hybrid nanofluid flow over curved stretching/shrinking surfaces.

The key research questions are:

- How do magnetic field, nonlinear mixed convection, and Darcy-Forchheimer effects modify Casson tetra-hybrid nanofluid flow behavior?
- What influence do homogeneous and heterogeneous reaction mechanisms have on the concentration distribution?
- Which nanoparticle combination yields the greatest improvement in heat transfer performance?
- How many simultaneous solutions exist for the governing equations?
- What are the stability characteristics of identified dual solutions?
- The major contributions and novelty of this work are summarized as follows:
- Investigation of dual solutions and their stability for Casson tetra-hybrid nanofluid flow (Cu + Al_2O_3 + Ag + TiO_2 / H_2O) over a curved surface.
- Comprehensive analysis of magnetohydrodynamic, nonlinear mixed convection, and homogeneous–heterogeneous reaction effects on the flow and thermal fields.
- Incorporation of the Darcy-Forchheimer porous medium model coupled with the Tiwari–Das nanofluid model to assess enhanced heat transfer capability.

Cu and Ag nanoparticles provide superior thermal conductivity, while Al_2O_3 and TiO_2 contribute to improved flow stability and heat transport characteristics [37]. These combined attributes make the present investigation well-suited for applications in thermal energy systems, electronics cooling, automotive heat exchangers, and other advanced industrial processes. Accordingly, this work focuses on examining how porosity affects the deformation behavior of Casson tetra-hybrid nanofluid flow past a porous curved surface, with special consideration of deformable surface roughness and the presence of homogeneous-heterogeneous chemical reactions.

Mathematical Analysis

Flow Description: This study examines a two-dimensional, steady, incompressible nonlinear mixed convection flow of a Casson tetra-hybrid nanofluid over a porous curved stretching/shrinking surface. A stability analysis is performed to assess the dual solutions that arise under certain physical conditions. The flow is subjected to homogeneous and heterogeneous chemical reactions occurring simultaneously within the fluid and on the surface. The curved surface is assumed to stretch or shrink with a velocity uw(s), where a > 0 is a constant controlling the stretching/shrinking rate. A mass flux velocity vw is imposed at the boundary to regulate suction or injection. A curvilinear coordinate system (r, s) is employed, with their-axis oriented normal to the flow and the s-axis tangential to the curved surface. Additionally, a transverse uniform magnetic field of strength B0 is applied perpendicular to the flow direction. The Tiwari-Das nanofluid model is adopted to account for nanoparticle volume fraction and thermal enhancement. The porous medium characteristics are incorporated using the Darcy-Forchheimer model to account for inertial resistance. The tetra-hybrid nanofluid is composed of a base fluid (water, H_2O) containing dispersed nanoparticles of Cu, Ag, TiO_2 and Al_2O3 providing superior heat transfer performance. Two reacting species, A and B, are considered to represent the chemical processes. The homogeneous reaction follows cubic autocatalysis, expressed as

$A + 2B \rightarrow 3B$, $r_h = K_1 b_1 b_2^2$ (a)

while the heterogeneous reaction takes place at the catalyst surface as

$A \rightarrow B$, $r_s = K_2 b_1$ (b)

where b_1 and b_2 denote the concentrations of species A and B, respectively and K_1, K_2 are the associated reaction rate constants [23]. The following figure illustrates the overall physical configuration of the problem.

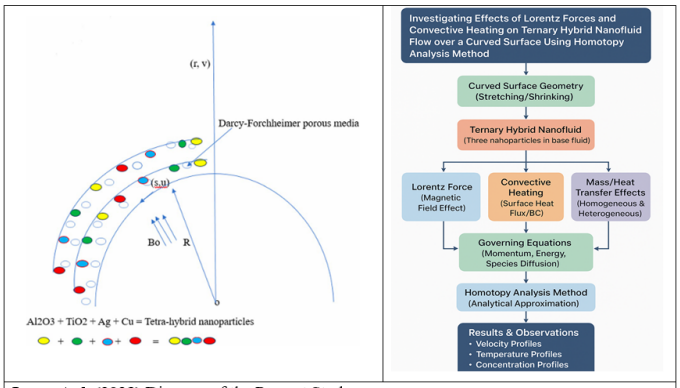

Lone et al. (2023) Diagram of the Present Study

Flow Model

The rheological behavior of a Casson fluid is described by the following equation [38–40]:

$$\tau_{ij} = \begin{bmatrix} 2e_{ij}\left\{\mu_B + \dfrac{P_y}{\sqrt{2\pi}}\right\}; \pi > \pi_c \\ 2e_{ij}\left\{\mu_B + \dfrac{P_y}{\sqrt{2\pi}}\right\}; \pi < \pi_c \end{bmatrix} \quad (1)$$

Here, represents the (i, j) – th component of the deformation rate tensor, $\pi = e_{ij}e_{ij}$ is the second invariant of the deformation rate tensor, μ_B is the plastic dynamic viscosity of the Casson fluid, is the critical value of P denotes the yield stress, τ_{ij} is the stress tensor and π_c is the critical value of π in the non-Newtonian model. From Eq. (1), the Casson fluid model can be simplified as:

$$\tau_{ij} = 2\mu_B e_{ij}\left(\frac{\beta+1}{\beta}\right) \quad (2)$$

where the Casson fluid parameter is defined as

$$\beta = \frac{\mu_B\sqrt{2\pi_c}}{P_y} \quad (3)$$

Governing Equations and Boundary Conditions of Flow Model Governing equations of the present study are given that follow (see [23, 36]):

$$\frac{\partial u}{\partial s}R = -\frac{\partial\left[v(R+r)\right]}{\partial r} \quad (4)$$

$$\frac{u^2}{R+r} = \frac{1}{\rho_{tethnf}}\frac{\partial P}{\partial r} \quad (5)$$

$$u\frac{\partial u}{\partial s}\frac{R}{r+R} + \frac{\partial T}{\partial r}v + \frac{vu}{r+R} + \frac{\sigma_{tethnf}B_0^{\,2}}{\rho_{tethnf}}u - \frac{g(\rho\omega)_{tethnf}}{\rho_{tethnf}}\left\{\gamma_1(T-T_\infty) + \gamma_2(T-T_\infty)^2\right\}$$

$$= \frac{\mu_{tethnf}}{\rho_{tethnf}}\left(\frac{1}{\beta}+1\right)\left[\frac{1}{r+R}\frac{\partial u}{\partial r} + \frac{\partial^2 u}{\partial r^2} - \frac{u}{(r+R)^2}\right] - \frac{\mu_{tethnf}}{\rho_{tethnf}}\left(\frac{1}{\beta}+1\right)\frac{u}{K^*} - \frac{1}{\rho_{tethnf}}\frac{Cb}{\sqrt{K^*}} - \frac{1}{\rho_{tethnf}}\frac{\partial P}{\partial s}\frac{R}{r+R} \quad (6)$$

$$u\frac{\partial T}{\partial s}\frac{R}{r+R} = \frac{K_{tethnf}}{(\rho C_p)_{tethnf}}\left\{\frac{1}{r+R}\frac{\partial T}{\partial r} + \frac{\partial^2 T}{\partial r^2}\right\} - \frac{\partial T}{\partial r}v \quad (7)$$

$$u\frac{\partial b_1}{\partial s}\frac{R}{r+R} = D_A\left(\frac{\partial^2 b_1}{\partial r^2} + \frac{1}{r+R}\frac{\partial b_1}{\partial r}\right) - K_i b_1 b_2^{\,2} - \frac{\partial b_1}{\partial r}v \quad (8)$$

$$u\frac{\partial b_2}{\partial s}\frac{R}{r+R} = D_B\left(\frac{\partial^2 b_2}{\partial r^2} + \frac{1}{r+R}\frac{\partial b_2}{\partial r}\right) - K_i b_1 b_2^{\,2} - \frac{\partial b_2}{\partial r}v \quad (9)$$

With their associated boundary conditions are (see [23, 36]):

$$k_f\frac{\partial T}{\partial r} = h_f(T_f - T) \quad (10a)$$

$$u = L\left\{\frac{\partial u}{\partial r} - \frac{u}{r+R}\right\} + \lambda as\ and\ v = v_w \quad (10b)$$

$$D_B\frac{\partial b_2}{\partial r} = -K_j b_2 \quad (10c)$$

$$D_A \frac{\partial b_1}{\partial r} = -K_j b_1 \tag{10d}$$

$$\text{asr} = 0 \tag{10e}$$

$$\frac{\partial u}{\partial r} \to 0, u \to 0, b_1 \to b_0, T \to T_\infty, asr \to \infty \tag{10f}$$

Where $\lambda < 0$ shrinking and $\lambda >$ stretching parameter
Thermo-Physical Properties of Tetra-Hybrid Nanofluid:
Mathematical formulas of tetra-hybrid nanofluid with their thermo-physical proper ties are listed as the following: (see [41] and [42]).

$$\rho\omega_{tethnf} = \phi4(\rho\omega)s4 + (1-\phi4)[(1-\phi3)[((1-\phi2)(1-\phi1)(\rho\omega)_f + \phi1(\rho\omega)s1) + \phi2(\rho\omega)s2] + \phi3(\rho\omega)s3],$$

$$\frac{\mu_{tethnf}}{\mu_f} = \frac{1}{(1-\phi1)^{\frac{5}{2}}(1-\phi2)^{\frac{5}{2}}(1-\phi3)^{\frac{5}{2}}(1-\phi4)^{\frac{5}{2}}},$$

$$\frac{\sigma_{nf}}{\sigma f} = \frac{\sigma s1 + (sf-1)\sigma f - (sf-1)\phi1(\sigma f - \sigma s1)}{\sigma s1 + (sf-1)\sigma f + \phi1(\sigma f - \sigma s1)},$$

$$\frac{\sigma_{hnf}}{\sigma nf} = \frac{\sigma s2 + (sf-1)\sigma nf - (sf-1)\phi2(\sigma nf - \sigma s2)}{\sigma s2 + (sf-1)\sigma nf + \phi2(\sigma nf - \sigma s2)},$$

$$\frac{\sigma_{trihnf}}{\sigma hnf} = \frac{\sigma s3 + (sf-1)\sigma hnf - (sf-1)\phi3(\sigma hnf - \sigma s3)}{\sigma s3 + (sf-1)\sigma hnf + \phi3(\sigma hnf - \sigma s3)},$$

$$\frac{\sigma_{tethnf}}{\sigma trihnf} = \frac{\sigma s4 + (sf-1)\sigma trihnf - (sf-1)\phi4(\sigma trihnf - \sigma s4)}{\sigma s4 + (sf-1)\sigma trihnf + \phi4(\sigma hnf - \sigma s4)},$$

$$\rho_{tethnf} = \phi4\rho s4 + (1-\phi4)[(1-\phi3)[((1-\phi2)(1-\phi1)\rho_f + \phi1\rho s1) + \phi2\rho s2] + \phi3\rho s3],$$

$$\frac{K_{nf}}{Kf} = \frac{Ks1 + (sf-1)Kf - (sf-1)\phi1(Kf - Ks1)}{Ks1 + (sf-1)Kf + \phi1(Kf - Ks1)},$$

$$\frac{K_{hnf}}{Knf} = \frac{Ks2 + (sf-1)Knf - (sf-1)\phi2(Knf - Ks2)}{Ks2 + (sf-1)Knf + \phi2(Knf - Ks2)},$$

A true "3D solution" here typically means **visualizing how one property varies with two independent parameters** (e.g., volume fractions). Since the full system is too large to solve analytically in closed form, we generate **3D surface plots**.

Step 1: Choose a Target Equation
For 3D visualization, pick one expression. For example:

$$\frac{\mu_{tethnf}}{\mu_f} = \frac{1}{(1-\phi_1)^{2.5}(1-\phi_2)^{2.5}(1-\phi_3)^{2.5}(1-\phi_4)^{2.5}}$$

We can visualize:
- X-axis → ϕ_1
- Y-axis → ϕ_2
- Z-axis → μ_{tethnf}/μ_f
- (Fix ϕ_3, ϕ_4)

Step 2: 3D Surface Interpretation

This shows how viscosity ratio grows as nanoparticle volume fractions increase.

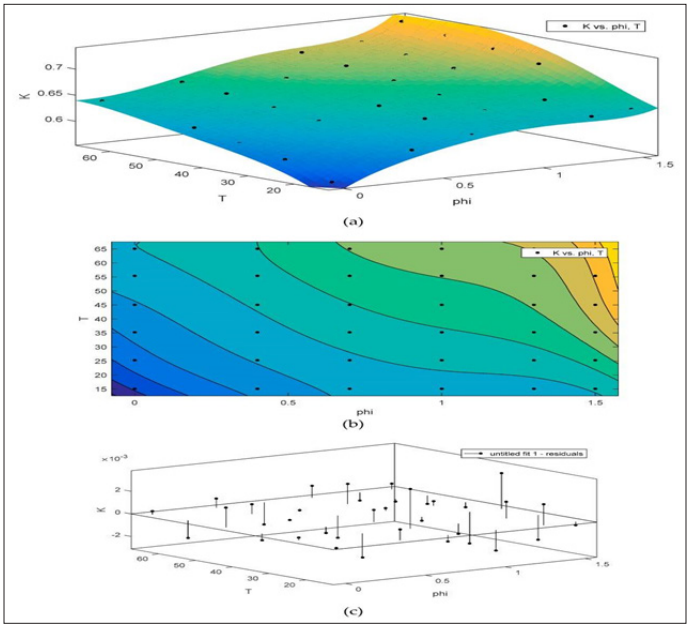

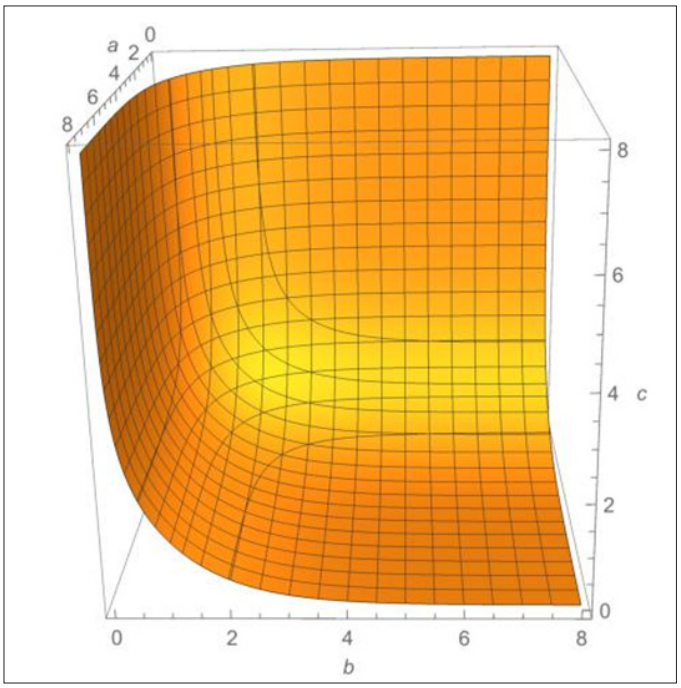

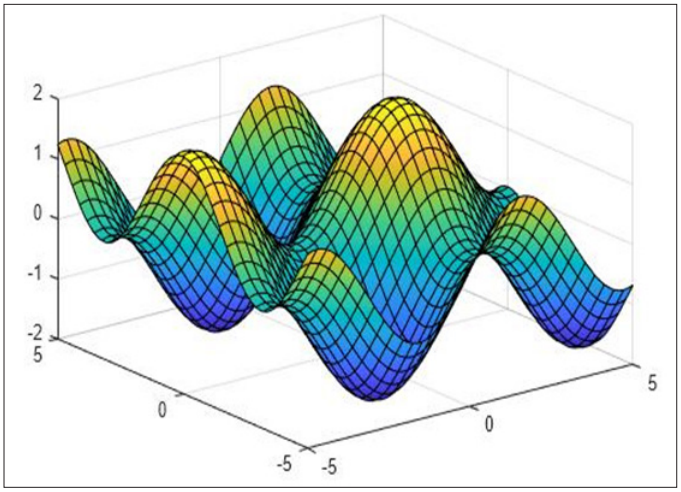

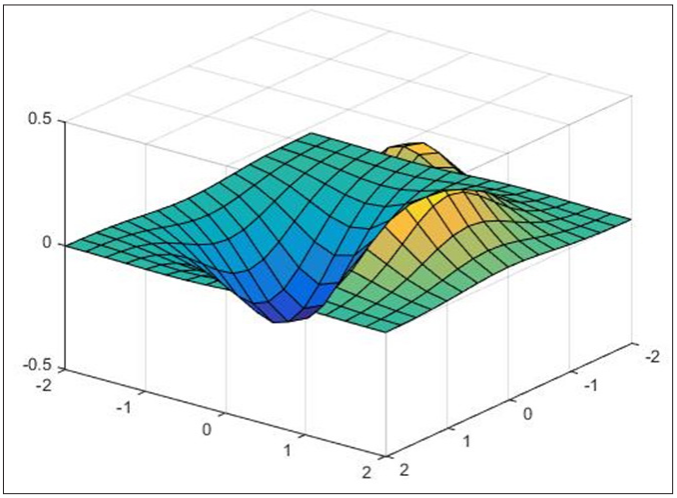

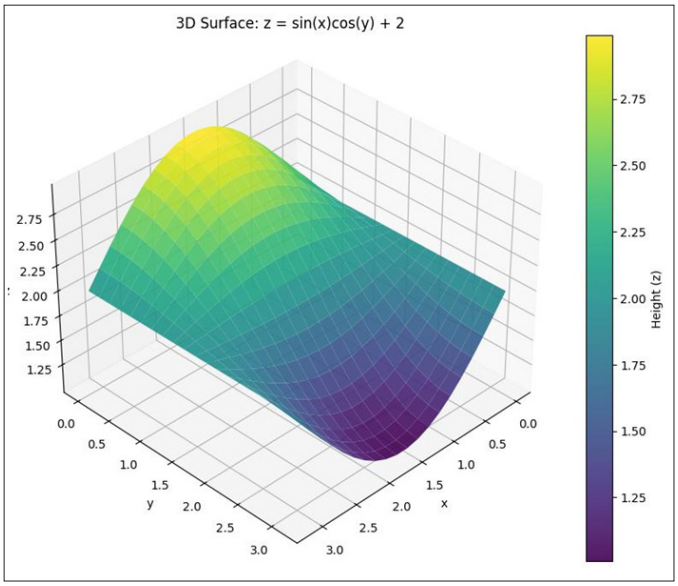

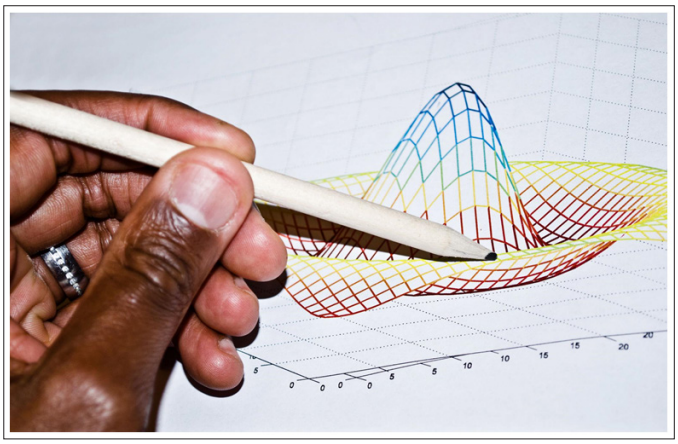

Key Insight

- As $\phi i\uparrow$, denominator $\downarrow \rightarrow$ viscosity $\uparrow$ sharply
- Nonlinear growth (very important in squeezing flow problems)

Step 3: Example MATLAB / Python Code for 3D Solution

MATLAB Code

```
phi1 = linspace(0,0.3,50);
phi2 = linspace(0,0.3,50);
[Phi1,Phi2] = meshgrid(phi1,phi2);
phi3 = 0.1;
phi4 = 0.1;
Z = 1 ./ ((1-Phi1).^(2.5) .* (1-Phi2).^(2.5) .* (1-phi3).^(2.5) .*
```

```
(1-phi4).^(2.5));
surf(Phi1, Phi2, Z)
xlabel('\phi_1'), ylabel('\phi_2'), zlabel('\mu_{hnf}/\mu_f')
title('3D Surface Plot of Viscosity Ratio')
```

Python (Matplotlib)

```
import numpy as np
import matplotlib.pyplot as plt
phi1 = np.linspace(0,0.3,50)
phi2 = np.linspace(0,0.3,50)
Phi1, Phi2 = np.meshgrid(phi1, phi2)
phi3 = 0.1
phi4 = 0.1
Z = 1 / ((1-Phi1)**2.5 * (1-Phi2)**2.5 * (1-phi3)**2.5 * (1-phi4)**2.5)
fig = plt.figure()
ax = fig.add_subplot(111, projection='3d')
ax.plot_surface(Phi1, Phi2, Z)
ax.set_xlabel('phi1')
ax.set_ylabel('phi2')
ax.set_zlabel('mu ratio')
plt.show()
```

Step 4: Extend to Your Research Model

You can generate similar 3D plots for:

- σhnf/σf → electrical conductivity
- Khnf/Kf → thermal conductivity
- ρtethnf → density variation

Research Insight (Important)

For your **MoS_2–SiO_2 hybrid nanofluid squeezing flow study:**

- 3D plots help show interaction effects
- Useful for:
  - Optimization (max heat transfer vs viscosity penalty)
  - Comparing mono vs hybrid nanofluids

Step 1: Select Core Equation (Thermal Conductivity)

We focus on your final hybrid stage:

$$\frac{K_{tethnf}}{K_{trihnf}} = \frac{K_{s4} + (s_f - 1)K_{trihnf} - (s_f - 1)\phi_4[K_{trihnf} - K_{s4}]}{K_{s4} + (s_f - 1)K_{trihnf} + \phi_4[K_{trihnf} - K_{s4}]}$$

Step 2: Define 3D Variables

To construct a surface:

- **X-axis** → ϕ_1 (3rd nanoparticle fraction)
- **Y-axis** → ϕ_4 (4th nanoparticle fraction)
- **Z-axis** → K_{tethnf}/K_f

We treat:

- ϕ_1, ϕ_2 = constants
- Material constants K_{si}, K_f fixed

Step 3: 3D Surface Behavior

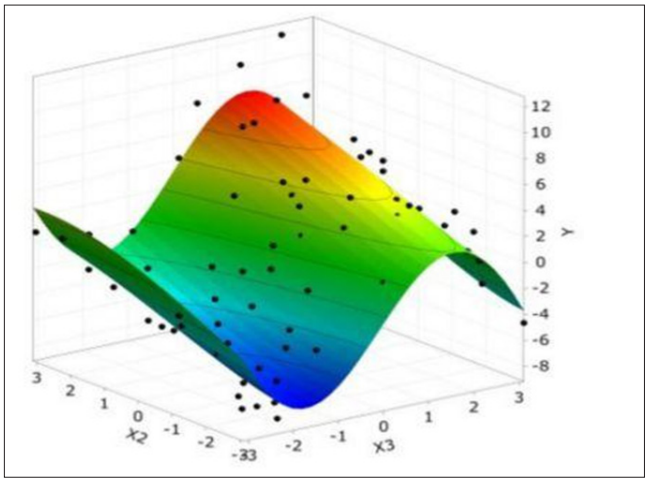

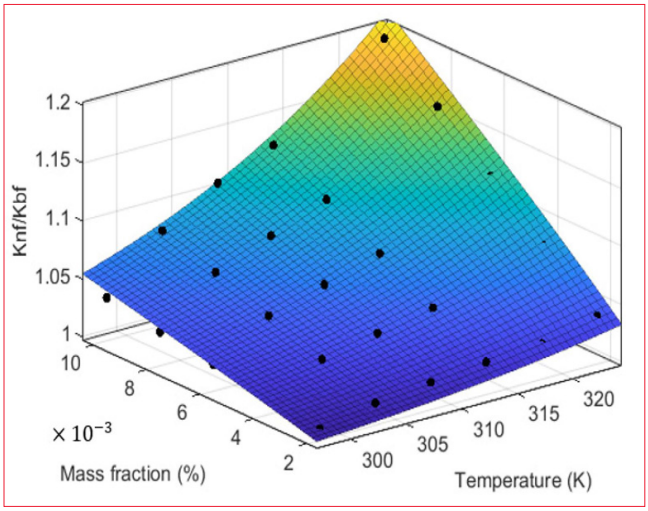

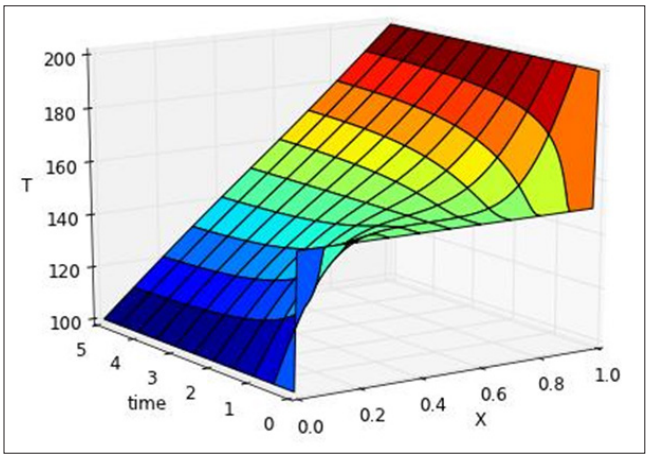

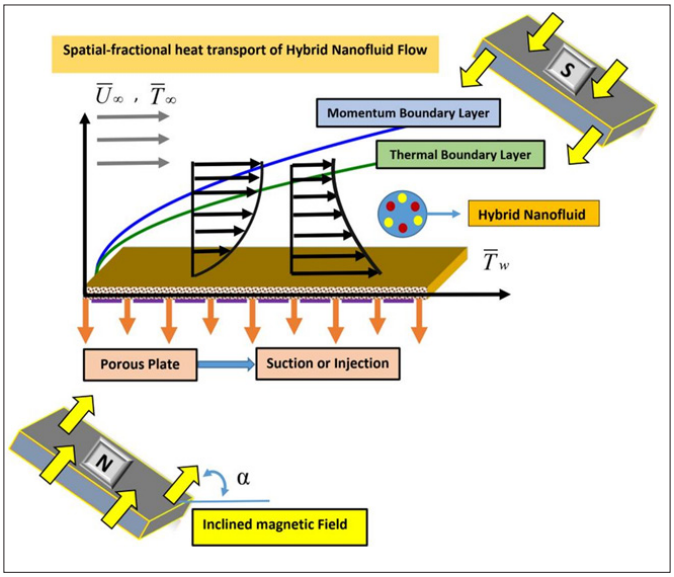

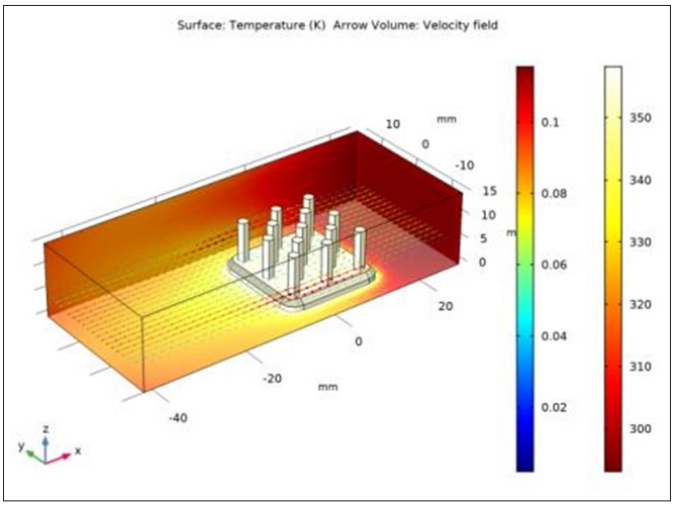

Interpretation

- Increasing ϕ_3, ϕ_4 → **thermal conductivity increases**
- Strong **nonlinear coupling** between hybrid particles
- Surface typically:
  - o Convex upward
  - o Steeper for high conductivity nanoparticles (MoS_2)

Step 4: MATLAB Code for 3D Solution

```
phi3 = linspace(0,0.3,50);
phi4 = linspace(0,0.3,50);
[Phi3,Phi4] = meshgrid(phi3,phi4);
% Constants (example values)
Ks4 = 15;
Ktrihnf = 10;
Khnf = 8;
sf = 1.2;
Z = (Ks4 + (sf-1)*Ktrihnf - (sf-1).*Phi4.*(Ktrihnf - Ks4)) ./ ...
(Ks4 + (sf-1)*Ktrihnf + Phi4.*(Khnf - Ks4));
surf(Phi3, Phi4, Z)
xlabel('\phi_3')
ylabel('\phi_4')
zlabel('K_{tethnf}/K_{trihnf}')
title('3D Thermal Conductivity Surface')
```

Step 5: Python Code

```
import numpy as np
import matplotlib.pyplot as plt
phi3 = np.linspace(0,0.3,50)
phi4 = np.linspace(0,0.3,50)
Phi3, Phi4 = np.meshgrid(phi3, phi4)
Ks4 = 15
Ktrihnf = 10
Khnf = 8
sf = 1.2
Z = (Ks4 + (sf-1)*Ktrihnf - (sf-1)*Phi4*(Ktrihnf - Ks4)) / \ (Ks4
+ (sf-1)*Ktrihnf + Phi4*(Khnf - Ks4))
fig = plt.figure()
ax = fig.add_subplot(111, projection='3d')
ax.plot_surface(Phi3, Phi4, Z)
ax.set_xlabel('phi3')
ax.set_ylabel('phi4')
ax.set_zlabel('K ratio')
plt.show()
```

Step 6: Research-Level Insight

For your **MoS_2–SiO_2 hybrid nanofluid study**:

- ϕ_3 → secondary nanoparticle (SiO_2)
- ϕ_4 → tertiary enhancement stage
- 3D plot reveals:
- **Optimal hybrid ratio**
- Trade-off between conductivity & viscosity
- Justification for **hybrid superiority over mono nanofluid**

$$\frac{K_{trihnf}}{Khnf} = \frac{Ks3 + (sf-1)Khnf - (sf-1)\phi3(Khnf - Ks3)}{Ks3 + (sf-1)Khnf + \phi3(Khnf - Ks3)},$$
$$\frac{K_{tethnf}}{Ktrihnf} = \frac{Ks4 + (sf-1)Ktrihnf - (sf-1)\phi4(Ktrihnf - Ks4)}{Ks4 + (sf-1)Ktrihnf + \phi4(Khnf - Ks4)}, \quad (11)$$
$$(\rho Cp)_{tethnf} = \phi4(\rho Cp)s4 + (1-\phi4)[(1-\phi3)[((1-\phi2)(1-\phi1)(\rho Cp)_f + \phi1(\rho Cp)s1) + \phi2(\rho Cp)s2] + \phi3(\rho Cp)s3].$$

The base fluid and nanoparticles, along with their thermophysical properties as reported by [43, 44], are presented in the following graphical figure. In this study, the notations represent the following:

- σ_{nf}, σ_{hnf}, σ_{trihnf}: electrical conductivity of the nanofluid, hybrid nanofluid, and trihybrid nanofluid, respectively.
- ρ_{nf}, ρ_{hnf}, ρ_{trihnf} : density of the nanofluid, hybrid nanofluid, and trihybrid nanofluid, respectively.
- k_{nf}, k_{hnf}, k_{trihnf}: thermal conductivity of the nanofluid, hybrid nanofluid, and trihybrid nanofluid, respectively.
- ω_{nf}, ω_{hnf}, ω_{trihnf}: thermal expansion coefficient of the nanofluid, hybrid nanofluid, and trihybrid nanofluid, respectively.
- C_{pnf}, C_{phnf}, $C_{ptrihnf}$: heat capacity of the nanofluid, hybrid nanofluid, and trihybrid nanofluid, respectively.
- μ_{nf}, μ_{hnf}, μ_{trihnf}: dynamic viscosity of the nanofluid, hybrid nanofluid, and trihybrid nanofluid, respectively.

These parameters are essential for characterizing the thermophysical behavior of the different nanofluids used in this study.

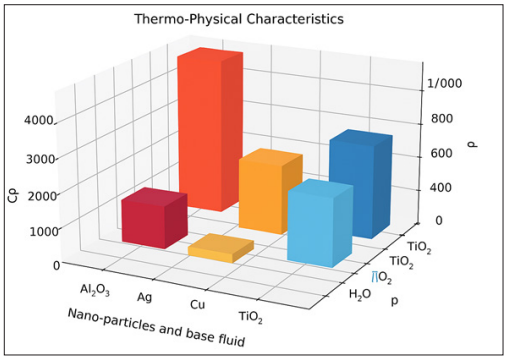

Normalization / Similarity transformations to simplify the analysis the following similarity transformations are used.

$$p = \rho_f a^2 s^2 P(\zeta), \quad b1 = b0h(\zeta), \quad b2 = b0\phi(\zeta), \quad K = R\sqrt{\frac{a}{\nu_f}},$$
$$v = -\frac{R}{r+R}\sqrt{a\nu_f} f(\zeta), \quad u = af'(\zeta)s, \quad \zeta = r\sqrt{\frac{a}{\nu_f}}, \quad \frac{\theta(\zeta)}{T-T_\infty} = \frac{1}{T_f - T_\infty}. \tag{12}$$

For the similarity solutions to exist, the applied mass flux velocity through the curved surface is given by:

$$-\sqrt{a\nu f}S = v_w \tag{13}$$

where, S indicates injunction (< 0) and suction (> 0) parameters.

After substituting Eq. (12) into Eq. (4)–(10), we get the following reduced form of governing equations.

$$\frac{\partial P}{\partial \zeta} = \frac{\rho_{tehnf}}{\rho_f}\frac{f'^2}{K+\zeta}, \tag{14}$$

$$\begin{aligned}&\frac{2K}{K+\zeta}P + \frac{\sigma_{tehnf}}{\sigma_f}Mf' - \frac{(\rho\omega)_{tehnf}}{(\rho\omega_f)}\lambda T1\theta(1+\lambda T2\theta)\\ &= \frac{\mu_{hnf}}{\mu_f}(1+\frac{1}{\beta})(\frac{f''}{K+\zeta} - 2\lambda i f' + f''' - \frac{f'}{(K+\zeta)^2})\\ &- \frac{\rho_{tehnf}}{\rho_f}(f'^2\frac{K}{K+\zeta} - \frac{K}{(K+\zeta)^2}f'f - \frac{K}{K+\zeta}f''f + 2Frf'^2),\end{aligned} \tag{15}$$

$$A16Pr\frac{K}{\zeta+K}f\theta' + A15(\theta'' + \frac{\theta'}{\zeta+K}) = 0, \tag{16}$$

$$\frac{K}{\zeta+K}fh + \frac{1}{Sc}(h'' + \frac{h'}{\zeta+K}) = Knh\phi^2, \tag{17}$$

$$\frac{K}{\zeta+K}f\phi + \frac{\delta}{Sc}(\phi'' + \frac{\phi'}{\zeta+K}) = Knh\phi^2. \tag{18}$$

with their respective boundary conditions are:

$$0 = f''(\infty), 0 = f'(\infty), f'(0) - \lambda = -A11\lambda 3(f''(0) - \frac{f'(0)}{K}), f(0) = S, \tag{19}$$

$$0 = \theta(\infty), -BiA15(1-\theta(0)) = \theta'(0), \phi(\infty) \to 0, \tag{20}$$

$$h(\infty) \to 1, kmh(0) = h'(0), kmh(0) = \delta\phi(0), \tag{21}$$

For both chemical species D and D (20) (21) diffusion coefficients are equal, such that 1= and thus

$$h(\zeta) = 1 - \phi(\zeta), \tag{22}$$

Then Eq. (17) and Eq. (18) yield

$$\frac{K}{\zeta+K}fh - Knh(1-h)^2 + (\frac{h'}{\zeta+K} + h'')\frac{1}{Sc} = 0, \tag{23}$$

with boundary condition as follows:

$$1 = h(\infty), Kmh(0) = h'(0). \tag{24}$$

By differentiating Eq. (15) with respect to following Eq. (25) and substituting in Eq. (14), we have the

$$-A12[\frac{K}{\zeta+K}(f''f'-f'''f)-\frac{K}{(\zeta+K)^2}(f'^2-f''f) \\ -\frac{K}{(\zeta+K)^3}f'f-2Fr(2f''f'+\frac{1}{(\zeta+K)^2}f'^2)]+ \tag{25}$$

$$A11(1+\frac{1}{\beta})[f^{iv}+f'''\frac{2}{\zeta+K}-f''\frac{1}{(\zeta+K)^2}+f'\frac{1}{(\zeta+K)^3}-2\lambda i(f''+\frac{1}{\zeta+K}f')] \\ -A13M(f''+\frac{1}{(\zeta+K)}f')+A14\lambda T1(\frac{\theta}{\zeta+K}+\theta'+\lambda T2\frac{\theta^2}{\zeta+K}+2\lambda T2\theta)=0 \tag{26}$$

Where $\frac{\mu_{tethnf}}{\mu_f}=A11$, $\frac{\rho_{tethnf}}{\rho_f}=A12$, $\frac{\sigma_{tethnf}}{\sigma_f}=A13$, $\frac{(\rho\omega)_{tethnf}}{(\rho\omega)_f}=A14$, $\frac{K_{tethnf}}{K_f}=A15$, $\frac{\rho Cp_{tethnf}}{\rho Cp_f}=A16$, $\beta=\mu f\frac{\sqrt{2\pi}}{Py}$, $Fr=\frac{Cb}{K^{*\frac{1}{2}}}$, $M=\frac{\sigma fBo^2}{\rho fa}$, $\lambda i=\frac{\nu f}{K^*}$, $Pr=\frac{\nu f}{\alpha f}$, $Sc=\frac{\nu f}{D_A}$, $Km=\frac{Kj}{D_A}\sqrt{\frac{\nu f}{a}}$, $Kn=\frac{KiCo^2}{a}$, $\lambda=\frac{a}{\nu f}s$, $Bi=\frac{hf}{kf}\frac{\nu f}{a}$, $\lambda 3=\sqrt{\frac{a}{\nu f}}$, $\lambda T1=\frac{Gr}{Re_s}$, $\lambda T2=\frac{\gamma 2(Tw-T\infty)}{\gamma 1}$, $Gr=\frac{g\gamma 1(Tw-T\infty)s^3}{\nu^2}$

The Physical Quantities Both surface Nu (Nusselt number) and Cf (shear stress) which are a critical measurable parameter of interest that quantifies the heat flux rate at the surface expressed as follows:

$$Nus=\frac{sqw}{(Tw-Tf)Kf},qw=-K_{tethnf}\frac{\partial T}{\partial r}, \\ Cf=\frac{\tau rs}{\rho fUw^2},\tau rs=-\mu_{tethnf}(1+\frac{1}{\beta})(\frac{\partial U}{\partial r}), \tag{27}$$

$$Re_s^{\frac{-1}{2}}Nu=-A15\theta'(0), \tag{28}$$

$$Re_s^{\frac{1}{2}}Cf=A11(1+\frac{1}{\beta})(-\frac{f'(0)}{K}+f''(0)), \tag{29}$$

where the local Reynolds number is represented by $Re_s=\frac{as^2}{\nu}$.

Stability Analysis

Res=as2 . (27) (28) (29) Referring to the work done by [45–47] on the stability analysis is important for the case of non uniqueness solution is present in this study. To identify the stability of this study some important steps are applied [48]. These steps are:

● introducing a new dimensionless time variables and similarity variables ● implement the linear eigenvalue equations and ● relax the boundary conditions.

New Similarity Transformation

First, we introduced τ (new dimensionless time variable) as the following [48]:

$$at=\tau \tag{30}$$

but, the similarity variables Eq. (12) are replaced by

$$v=-\frac{R}{r+R}f(\zeta,\tau)\sqrt{a\nu_f},\quad as\frac{\partial f}{\partial\zeta}(\zeta,\tau)=u,\quad \sqrt{\frac{a}{\nu_f}}r=\zeta, \\ b1=b0\phi(\zeta,\tau),b2=b0h(\zeta,\tau),\frac{T-T_\infty}{T_w-T_\infty}=\theta(\zeta,\tau),\rho_f a^2s^2P(\zeta,\tau)=p,R\sqrt{\frac{a}{\nu_f}}=K. \tag{31}$$

By putting Eq. (31) into the unsteady form of Eqs. (4)–(9) we get the following:

$$
\begin{aligned}
&-A12[\frac{K}{\zeta+K}(\frac{\partial f}{\partial \zeta}\frac{\partial^2 f}{\partial \zeta^2}-f\frac{\partial^2 f}{\partial \zeta^2})-\frac{K}{(K+\zeta)^2}(\frac{\partial f}{\partial \zeta}^2-f\frac{\partial^2 f}{\partial \zeta^2})\\
&-\frac{K}{(K+\zeta)^3}f\frac{\partial f}{\partial \zeta}-2Fr(2\frac{\partial^2 f}{\partial \zeta^2}\frac{\partial f}{\partial \zeta}+\frac{1}{(\zeta+K)^2}\frac{\partial f}{\partial \zeta}^2)]\\
&+A11(1+\frac{1}{\beta})[\frac{\partial^4 f}{\partial \zeta^4}+\frac{2}{\zeta+K}\frac{\partial^3 f}{\partial \zeta^3}-\frac{1}{(K+\zeta)^2}\frac{\partial^2 f}{\partial \zeta^2}\\
&-\frac{1}{(K+\zeta)^3}\frac{\partial f}{\partial \zeta}-2\lambda(\frac{\partial^2 f}{\partial \zeta^2}+\frac{1}{\zeta+K}\frac{\partial f}{\partial \zeta})]-A13M(\frac{\partial^2 f}{\partial \zeta^2}+\frac{1}{(\zeta+K)}\frac{\partial f}{\partial \zeta})\\
&+A14\lambda T1(\frac{\theta}{\zeta+K}+\frac{\partial \theta}{\partial \zeta}+\lambda T2\frac{\theta^2}{\zeta+K}+2\lambda T2\theta)\\
&-\frac{1}{(K+\xi)}\frac{\partial^2 f}{\partial \xi \partial \tau}-\frac{\partial^3 f}{\partial \zeta^2 \partial \tau}=0
\end{aligned}
\tag{32}
$$

$$
A16Pr\frac{K}{\zeta+K}f\frac{\partial \theta}{\partial \zeta}+A15(\frac{\partial^2 \theta}{\partial \zeta^2}+\frac{1}{\zeta+K}\frac{\partial \theta}{\partial \zeta})-\frac{\partial \theta}{\partial \tau}=0 \tag{33}
$$

$$
\frac{K}{\zeta+K}hf-(1-h)^2Knh+(\frac{\partial^2 h}{\partial \zeta^2}+\frac{1}{\zeta+K}\frac{\partial h}{\partial \zeta})\frac{1}{Sc}-\frac{\partial h}{\partial \tau}=0 \tag{34}
$$

with their respective boundary conditions are:

$$
\begin{aligned}
&\frac{\partial^2 f}{\partial \zeta^2}(\infty,\tau)=0,\frac{\partial f}{\partial \zeta}(\infty,\tau)=0,S=f(0,\tau),\frac{\partial f}{\partial \zeta}(0,\tau)\\
&-\lambda=-A11\lambda 3(\frac{\partial^2 f}{\partial \zeta^2}(0,\tau)-\frac{1}{K}\frac{\partial f}{\partial \zeta}(0,\tau)),
\end{aligned}
\tag{35}
$$

$$
0=\theta(\infty,\tau),\frac{\partial \theta}{\partial \zeta}(0,\tau)+BiA15(1-\theta(0,\tau))=0, \tag{36}
$$

$$
1=h(\infty,\tau),\frac{\partial h}{\partial \zeta}(0,\tau)-Kmh(0,\tau)=0, \tag{37}
$$

Introducing Linear Eigenvalue Equations

The stability of the steady flow solution can be expressed by setting of $h(\zeta)=h_0(\zeta)$, $\theta_0(\zeta)=\theta(\zeta)$ and $f_0(\zeta)=f(\zeta)$ where it satisfied the boundary value problems as Eq. (32)- Eq. (37). Thus, [46] initialized the following equations.

$$
\begin{aligned}
&h(\zeta,\tau)=e^{-\gamma\tau}H(\zeta,\tau)+h_0(\zeta),\quad \theta(\zeta,\tau)=e^{-\gamma\tau}\theta_1(\zeta,\tau)+\theta_0(\zeta)\quad f(\zeta,\tau)\\
&=e^{-\gamma\tau}F(\zeta,\tau)+f_0(\zeta).
\end{aligned}
\tag{38}
$$

where, unknown eigenvalue parameter is γ and the functions $H(\zeta,\tau)$, $\theta_1(\zeta,\tau)$ and $F(\zeta,\tau)$ are relatively small compared to $h_0(\zeta)$, $\theta_0(\zeta)$ and $f_0(\zeta)$ respectively.

By setting (38) in (32) - (37) and consider $0=\tau$ we get the following (see [36]):

$$
\begin{aligned}
&A12[-\frac{K}{(\zeta+K)^2}(f0F''+f0''F)+\frac{K}{\zeta+K}(f0F'''+f0'''F)\\
&-\frac{K}{(\zeta+K)^3}(f0F'+f0'F)-\frac{K}{\zeta+K}(F''f0'+f0''F')\\
&-\frac{K}{(\zeta+K)^2}(2F'f0')+\frac{Fr}{A2}(2F''f0'+f0'F')+\frac{1}{\zeta+K}(2F'f0')]\\
&+A11(\frac{1}{\beta}+1)[F^{iv}+\frac{2}{\zeta+K}F'''-\frac{1}{(\zeta+K)^3}F'\\
&-\frac{1}{(\zeta+K)^2}F''-2\lambda(\frac{1}{\zeta+K}F'+F'')]+A13M(F''+\frac{F'}{\zeta+K})\\
&+\lambda T1A14[\lambda T2\theta0'\theta1'+\theta1'(1+\lambda T2\theta0)+\theta0\theta1']\\
&+\frac{\gamma}{\zeta+K}F'+\gamma F''=0,
\end{aligned}
\tag{39}
$$

$$
\begin{aligned}
&A16\frac{K}{\zeta+K}(\theta1'f0-\theta1f0'+\theta0'F-\theta0'F')+\theta1\gamma\\
&+\frac{A15}{Pr}(\theta1''+\frac{\theta1'}{\zeta+K})=0,
\end{aligned}
\tag{40}
$$

$$
\frac{K}{\zeta+K}\left[f_0H'+Fh\right]-K_n\left\{1-4h+3h^2\right\}H+\gamma H+\frac{1}{S_c}\left\{H''+\frac{H'}{\zeta+K}\right\}=0 \tag{41}
$$

With their respective boundary conditions

Boundary Conditions (Equation 42)
$\theta_1'(0) = (Bi/A_{15})\theta_1(0)$, $H'(0) = K_m H(0)$, $F(0) = 0$,
$F'(0) = \lambda_3(-F'(0)K^{-1} + F''(0))$, $\theta_1(\infty) = 0$, $H(\infty) = 0$, $F''(\infty) = 0$, $F'(\infty) = 0$.

Relaxation of Boundary Conditions
The relaxation of boundary conditions is implemented to perform the stability analy sis, following the approach proposed by Harris et al. [47]. Specifically, the condition F′′(∞ is replaced by F′′′ in such cases. The unbounded set of unknown eigenvalues must be determined under the new condition F′′′, together with the linearized boundary value problem Eqs. (39)-(42). If the resulting eigenvalue has a negative sign, the smallest eigenvalues correspond to unstable solutions, and the flow exhibits a tendency toward the growth of distur bances. Conversely, if the eigenvalue has a positive sign, the smallest eigenvalues correspond to stable solutions, and the flow shows an initial decay of perturbations.

Numerical Solution
The nonlinear ordinary differential equations Eq. (16), Eq. (23), and Eq. (25), sub ject to the boundary conditions Eq. (19), Eq. (20), and Eq. (24), are solved using the bvp4c solver in MATLAB. This solver has been widely employed by researchers to solve similar boundary value problems. It is based on a finite-difference scheme with fourth-order accuracy. To apply the solver effectively, the governing equations must first be transformed into an equivalent system of first-order ordinary differential equations. This reformulation is carried out as follows:

Transformation to First-Order System (Equation 43)
f′ = y2, f = y1, f′′′ = y4, f′′ = y3, fiv = y4′
θ′ = y6, θ′′ = y6′, θ = y5
h′′ = y8′, h = y7, h′ = y8
The syntax of this solver is given by sol=bvp4c(@OdeBVP,@ OdeBC,solinit,options) where @OdeBVP is the function handle that encodes the governing equations Eq. (16), Eq. (23), and Eq. (25), as defined in Eq. (43), and @OdeBC is the function handle that encodes the boundary conditions Eq. (19), Eq. (20), and Eq. (24), also described in Eq. (43). The bvp4c solver applies the three-stage Lobatto IIIa collocation method. This scheme produces collocation polynomials of fourth-order accuracy and ensures a C-continuous solution with uniform integration over the interval, as discussed by Bilal et al. [49]. For the stability analysis, the same procedure is followed. Specifically, the equa tions Eq. (39)–Eq. (41) together with the boundary conditions Eq. (42) are rewritten as a system of first-order ordinary differential equations by introducing suitable sub stitutions. Assume that,

System Transformation (Equation 44)
$F' = y_2$, $F = y_1$, $F''' = y_4$, $F'' = y_3$, $F^{iv} = y_4'$
$\theta_1' = y_6$, $\theta_1 = y5$, $\theta_1'' = y_6'$
$H' = y_8$, $H = y7$, $H'' = y_8'$

Initial Conditions (Equation 45)
$f0' = s_2$, $f_0 = s1$, $f_0''' = s_4$, $f_0'' = s_3$
$\theta_0' = s_6$, $\theta_0 = s_5$
$h_0 = s7$, $h0' = s_8$

Finally, Coding Eq. (44)-(45). So, from this coding the output is a smallest eigen value that we expect from the new first order ordinary differential equations into the solver.

Fruitful and Feasible Conclusions:

This study presents a numerical investigation of steady, two-dimensional, incompressible, nonlinear mixed convection flow of a **Casson tetra-hybrid nanofluid** over a **porous curved stretching/ shrinking surface** with **homogeneous and heterogeneous chemical reactions**. The governing equations were solved using the **MATLAB bvp4c** solver, and the stability of dual solutions was analyzed. The major findings can be summarized as follows:

- The parameters **F_r**, **λ**, and **β** exhibit similar influences on the velocity profile f'(ζ).
- The parameters **λ_T** and **λ_M** exert opposite effects on the velocity distribution f'(ζ).
- The **stretching / shrinking parameter (λ)** and the **magnetic parameter (M)** strongly affect the temperature field, showing contrasting behaviors.
- The **tetra-hybrid nanofluid ($\phi_1 + \phi_2 + \phi_3 + \phi_4$)** demonstrates superior **thermal conductivity** and **heat transfer efficiency** compared to tri-hybrid, hybrid, and conventional nanofluids.
- Increasing the **homogeneous (K_m)** and **heterogeneous (K_n)** reaction parameters decreases the concentration profile h(ζ), thereby reducing the dual-solution region.
- Increasing **S**, **λ**, and **λ_T** enhances the **skin friction coefficient** (**$C_f Re^{1/2}$**) for both branches of solutions.
- The same parameters (**S, λ, λ_T**, and **M**) enhance the **Nusselt number** (**$N_u Re^{-1/2}$**) for the first solution while reducing it for the second.
- Dual solutions are observed for both skin friction and heat transfer rate when $\lambda > \lambda_c$, influenced by parameters such as **F_r**, **K_m** and **λ_T**.
- The **tetra-hybrid nanofluid** yields the **highest heat transfer augmentation** compared to lower-order nanofluid models.
- Increasing **λ** reduces the streamline strength and fluid motion for both dual solutions.
- An increase in **M** amplifies the temperature gradients along the isothermal contours for both branches.
- **Grid independence tests** and **comparisons with published literature** confirm the **accuracy and robustness** of the numerical method.
- **Stability analysis** reveals that the **first (primary) solution is stable** (positive eigenvalue), while the **second (secondary) solution is unstable** (negative eigenvalue), for different values of the Casson parameter **β**.

Further Research and Future Scope

Building upon the present findings, several promising extensions can be explored in future work:

- **Unsteady Flow Analysis:** Investigate time-dependent effects on the stability and transition between multiple solutions.
- **Non-Newtonian Fluid Models:** Extend the analysis to other rheological models such as Williamson, Carreau or Cross fluids.
- **Triple or Multiple Solutions:** Examine conditions leading to triple or higher-order solutions to capture more complex bifurcation behavior.
- **Buongiorno Model:** Incorporate thermophoretic and Brownian diffusion effects using the Buongiorno nanofluid framework for more realistic transport modeling.
- **Entropy Generation Analysis:** Perform second-law thermodynamic (entropy) analysis to assess energy efficiency and irreversibility.
- **Complex Geometries:** Extend the model to diverse configurations such as **spherical**, conical, or wavy surfaces to simulate practical engineering and biomedical systems.
- **Hybrid Optimization:** Explore the influence of varying nanoparticle composition ratios to optimize thermal and flow characteristics.
- **Experimental Validation:** Complement numerical results with laboratory or industrial-scale experimental data for validation and practical relevance.

Declarations

Funding

This research did not receive any specific grant from funding agencies in the public, commercial, or not-for-profit sectors. The study was conducted independently without external financial support.

Author Contributions

The author solely contributed to the conception and design of the study, data collection, analysis, interpretation of results, and preparation of the manuscript. The author has read and approved the final version of the manuscript and agrees to be accountable for all aspects of the work.

Conflict of Interest

The author declares that there are no known competing financial interests or personal relationships that could have influenced, or could be perceived to have influenced, the work reported in this paper.

Data Availability Statement

the data utilized in this study were obtained from publicly accessible online sources. All relevant data supporting the findings of this study are available within the article or can be accessed from the respective public repositories cited in the manuscript.

Institutional Review Board (IRB) Statement

Not applicable. This study did not involve human participants, animal subjects, or any form of clinical experimentation requiring ethical approval.

Informed Consent Statement

Not applicable. The study does not involve human subjects or identifiable personal data.

Ethics Statement

This research adheres to standard academic and scientific ethical guidelines. The manuscript does not involve any procedures or content that raise ethical concerns.

Disclosure of AI Use

Artificial intelligence (AI) tools, including ChatGPT, were used in a limited capacity solely for language refinement, formatting, and improving the clarity of the manuscript. The intellectual content, analysis, and conclusions of the study remain the original work of the author.

Acknowledgement

The author would like to express sincere gratitude to their affiliated institution for providing a supportive academic environment to conduct this research. The author also acknowledges the use of publicly available data sources and scholarly materials that contributed to the completion of this study. Constructive insights from peers and reviewers are also gratefully acknowledged, as they helped enhance the quality and rigor of the manuscript.

References

1. Casson N (1959). Flow equation for pigment–oil suspensions of the printing ink type. Rheology of Disperse Systems: 84-104.
2. Merkin J (1986) Dual solutions in mixed convection in porous medium. Journal of Engineering Mathematics 20: 171-179.
3. Choi SU, Eastman JA (1995) Enhancing thermal conductivity of fluids with nanoparticles. Argonne National Laboratory. https://ecotert.com/pdf/196525_From_unt-edu.pdf.
4. Chaudhary M, Merkin J (1995) A simple isothermal model for homogeneous–heterogeneous reactions. Fluid Dynamics Research 16: 311-333.
5. Dash R, Mehta K, Jayaraman G (1996) Casson fluid flow in a pipe filled with a homogeneous porous medium. International Journal of Engineering Science 34: 1145-1156.
6. Das SK, Thiesen P, Roetzel W, Putra N (2003) Temperature dependence of thermal conductivity enhancement for nanofluids. Journal of Heat Transfer 125: 567-574.
7. Weidman P (2006) Transpiration effects on boundary-layer flow. International Journal of Engineering Science: 44.
8. (Note: Your early Patel & Deheri works from 2001–2005 are grouped below)
9. Deheri GM, Patel RMH (2001) Porous hyperbolic slider bearing. Prajna Journal https://www.spuvvn.edu/publication/prajna/prajna_2017/Prajna%20-2017%20volume%2024-25.pdf.
10. Patel RMH, Deheri GM (2002–2005) Multiple works on squeeze film lubrication, magnetic fluids, curved plates, annular plates, and porous bearings (Indian Journal of Engineering, Journal of Mathematics, Tribology, etc.).
11. Harris S (2009) Mixed convection in porous media. Transport in Porous Media.
12. Murali K, Naidu VK, Venkatesh B (2019) Darcy-Brinkman-Forchheimer FEM model. https://iopscience.iop.org/article/10.1088/1742-6596/1172/1/012033/pdf .
13. Khan MI (2020) Micropolar ferrofluid flow.
14. Izadi A (2020) CPU cooling using nanofluids.
15. Aghamajidi M, Yazdi ME, Dinarvand S, Pop I (2018) Tiwari–Das nanofluid model 7: 78-90.
16. Mishra S (2022) Entropy generation in nanofluids.
17. Wahid NS (2021) Hybrid nanofluid over curved surfaces.
18. Xia WF (2022) Multi-slip hybrid nanofluid.
19. Mishra A, Upreti H (2022) Comparative nanofluid models.
20. Varun Kumar (2022) Casson nanofluid modeling.
21. Lone SA (2023) Ternary hybrid nanofluid (HAM).
22. Yasmin H (2023) Gyrotactic microorganisms.
23. Ibrahim W, Gizewu T (2023) Stability analysis 13: 21676.
24. Hyder A (2025) early online context overlap.
25. Rana P (2019) but relevant to multi-solution HAM studies.
26. Bhargavi N, Poornima T (2024) Hydromagnetic Casson flow 10: e30638
27. Asghar A (2024) Ferrofluid & slip effects.
28. Sarma S (2024) Mixed convection hybrid nanofluid.
29. Shen M (2024) Hybrid nanofluid with reactions.
30. Soomro AM (2024) Stability in Casson nanofluid.
31. Deebani W (2025) Magnetized radiative Casson nanofluid.
32. Rehman A (2025) Darcy–Forchheimer CNT nanofluids.
33. Kumar P (2025) Casson–Carreau nanofluid.
34. Ramasekhar, Shah (2025) Biomedical nanofluid applications.
35. Asghar (2025) Dual solutions & thermal stability.
36. Hyder (2025) Ternary hybrid nanofluids.